ADVANCED MATERIALS INTERFACES
www.advmatinterfaces.de

Analyzing Interface Recombination in Lead-Halide Perovskite Solar Cells with Organic and Inorganic Hole-Transport Layers

*Jinane Haddad, Benedikt Krogmeier, Benjamin Klingebiel, Lisa Krückemeier, Stephanie Melhem, Zhifa Liu, Jürgen Hüpkes, Sanjay Mathur, and Thomas Kirchartz**

The interfaces between absorber and transport layers are shown to be critical for perovskite device performance. However, quantitative characterization of interface recombination has so far proven to be highly challenging in working perovskite solar cells. Here, methylammonium lead halide ($CH_3NH_3PbI_3$) perovskite solar cells are studied based on a range of different hole-transport layers, namely, an inorganic hole-transport layer CuO_x, an organic hole-transport layer poly(triarylamine) (PTAA), and a bilayer of CuO_x/PTAA. The cells are completed by a [6,6]-phenyl-C_{61}-butyric acid methyl ester (PCBM)/bathocuproine/Ag electron contact. Energy levels are characterized using photoelectron spectroscopy and recombination dynamics by combining steady-state photoluminescence and transient photoluminescence with numerical simulations. While the PTAA-based devices hardly show any interface recombination losses and open-circuit voltages >1.2 V, substantial losses are observed for the samples with a direct CuO_x/perovskite interface. These losses are assigned to a combination of energetic misalignment at the CuO_x/perovskite interface coupled with increased interface recombination velocities at the perovskite/PCBM interface.

1. Introduction

Nonradiative recombination is one of the most important physical mechanisms that limits the performance of optoelectronic and photovoltaic devices.[1,2] Materials showing slow nonradiative recombination are therefore highly sought after. In traditional semiconductors like Si and GaAs slow nonradiative recombination is achieved by using processes involving high processing temperatures or large crystal sizes (ideally single crystals) which then lead to low defect densities. Achieving similar electronic quality in solution processed semiconductors had been impossible until the class of lead-halide perovskites became the focus of scientific attention in photovoltaics and optoelectronics.[3–6] Lead-halide perovskites are a class of materials that can be processed from solution at room temperature and that achieve- if processed correctly- extremely low nonradiative recombination rates relative to the radiative recombination rates.[7,8] This enables fairly high external luminescence quantum efficiencies that may exceed 30% in films on glass,[8–10] 20% in light-emitting diodes,[11–13] and 5% in solar cells.[14,15] These high luminescence quantum efficiencies in films correspond to high charge-carrier concentrations under steady-state illumination and thereby to a high quasi-Fermi level splitting. Thus, the chemical potential of the electron–hole pairs and thus the high implied open circuit voltage in films can be very high due to the long charge-carrier lifetimes.[8] However, the application of transport layers often substantially reduces the open-circuit voltage measured at the external terminals of a photovoltaic device.[16–18] The reason for this voltage loss due to the application of transport layers is the recombination occurring at the interface between the perovskite absorber layer and the hole- and electron-transport layer. Suppressing interface recombination by interface passivation or modification of interfacial energetics has been central to several recent publications featuring high efficiency perovskite solar cells.[15,19–21]

From a fundamental, thermodynamic point of view, any interface recombination loss will have a contribution depending on the concentration and capture-cross sections of interface defects and a contribution that depends on the energy-level alignment of the absorber and the transport layers.[22,23] We show that the first contribution involving the kinetics of recombination causes an entropic loss, while the second contribution (the energy-level alignment) determines the enthalpy of the electron–hole pair at an interface. Both effects will then

J. Haddad, B. Krogmeier, Dr. B. Klingebiel, L. Krückemeier, S. Melhem, Dr. Z. Liu, Dr. J. Hüpkes, Prof. T. Kirchartz
IEK5-Photovoltaik
Forschungszentrum Jülich
Jülich 52425, Germany
E-mail: t.kirchartz@fz-juelich.de
Prof. S. Mathur
Institute of Inorganic Chemistry
University of Cologne
Greinstr. 6, Cologne 50939, Germany
Prof. T. Kirchartz
Faculty of Engineering and CENIDE
University of Duisburg-Essen
Carl-Benz-Str. 199, Duisburg 47057, Germany
The ORCID identification number(s) for the author(s) of this article can be found under https://doi.org/10.1002/admi.202000366.

DOI: 10.1002/admi.202000366

determine the maximum free energy of the electron–hole pairs and hence their open-circuit voltage.

Large band offsets cause charge carriers to accumulate close to the contact leading to increased recombination. Large defect densities and capture-cross sections increase the so-called surface-recombination velocity S_n that controls how fast a given concentration of charge carriers will recombine at a surface or interface.[24] Finding the ideal charge-transport layers for a given perovskite absorber is therefore a multidimensional problem requiring perfect energy-level alignment on both sides, low surface-recombination velocities, ideally combined with high stability and processability. This task is complicated by the fact that the conduction- and valence-band edge of perovskite absorbers varies with composition[25] implying that the right choice of charge-transport layer for one absorber material may not be the right choice for another. Therefore, characterization methods have to be developed that are able to assign the reasons for high or low performance to the correct interface and that distinguish between kinetic and energetic losses at interfaces.

Here we focus on providing a methodology to characterize and simulate interfaces between perovskite-absorber layers and charge-transport layers and thereby identify the origins of recombination losses at these interfaces. To achieve this task, we use a combination of photoelectron spectroscopy, steady-state and transient photoluminescence to characterize the interface energetics and recombination kinetics of a series of p–i–n type $CH_3NH_3PbI_3$ (methylammonium lead iodide, MAPI) solar cells that feature different hole-transport layers. The used cell stack is shown in **Figure 1**a and consists of a glass/indium tin oxide (ITO) superstrate, on which different hole-transport layers (HTL) are deposited. These are either poly(triarylamine) (PTAA) represented by the red color, CuO_x following the recipe of ref. [26] represented by the green color, or a bilayer of CuO_x and PTAA represented in blue. On these hole-transport layers, MAPI is deposited using a $Pb(CH_3COO)_2$ (lead acetate):$PbCl_2$ (lead chloride) based process recently described in ref. [14] and in the Experimental Section. The electron-transport layer (ETL) is [6,6]-phenyl-C_{61}-butyric acid methyl ester (PCBM) followed by spin-coated bathocuproine (BCP) and an evaporated Ag back contact. The choice of PTAA as a hole-transport layer provides an extremely low surface-recombination velocity at the interface between the PTAA and the MAPI as shown in ref. [14]. The good front interface in this stack in combination with the PCBM/BCP/Ag back contact allows fairly high open-circuit voltages well above 1.2 V (see Figure 1b). However, the high resistivity of the PTAA leads to increased series resistances that lead to substantial fill factor *FF* losses;[27,28,29] in one case 6% absolute *FF* loss resulted from a mere 10 nm increase of PTAA thickness (see e.g. Figure 5 in ref. [27]). In the aim to reduce cost and increase the *FF* we investigate inorganic HTLs. Typically, NiO_x is the commonly used inorganic HTL[30] especially in nanoparticle form. Nevertheless, medical studies have shown the toxic effect of these nanoparticles, where they are related to the modification of cells in the respiratory tracks and also related to breast cancer in humans.[31,32] Therefore, they are not ideal for solar cell industrialization. An alternative to NiO_x could be an extremely thin layer of CuO_x, which has been proposed in several publications.[26,33–42] A particularly promising result was published by Rao et al.[26] who demonstrated CuO_x-based MAPI solar cells with an efficiency of 19%. In this work, we therefore investigate CuO_x as an alternative to the organic molecule PTAA to better understand the interface-recombination losses in our devices. Before delving into the analysis of recombination rates and interfacial energetics, we first study the properties of the ITO layer coated with the copper acetyl-acetonate ($Cu(acac)_2$) salt dissolved in dichlorobenzene (DCB) prepared as described by Rao et al.[26]

2. Results

2.1. Material Characterization for the CuO_x

Following the recipe of the CuO_x process solution process as described in refs. [26,38,39], we prepare the CuO_x layers on

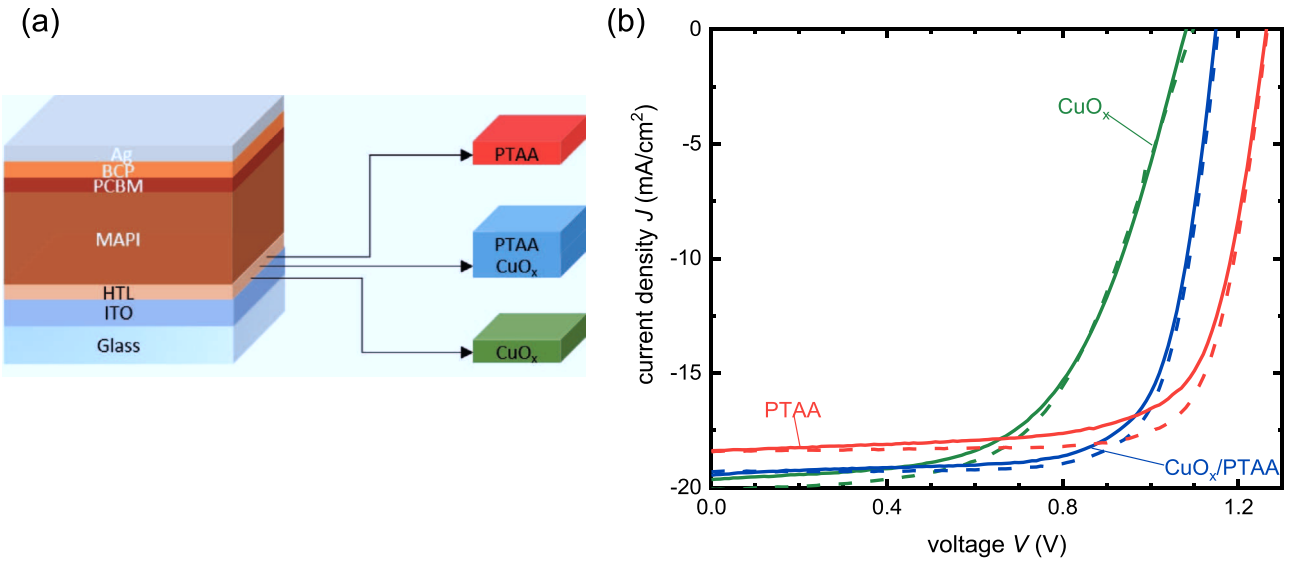

Figure 1. a) Schematic illustration of the device stack with three different hole-transport layers. b) Current density *J* as a function of voltage *V* under a class AAA solar simulator. Solid lines are for forward scans from short-circuit current J_{sc} to open-circuit voltage V_{oc} and dashed lines for reverse scans.

ITO-coated substrates by spin-coating $Cu(acac)_2$ salt in DCB solution with a concentration of 1.5 mg mL^{-1} followed by an annealing in air at 80 °C and a methanol wash. However, scanning-electron microscopy reveals that this recipe does not lead to CuO_x layers that can easily be identified on the ITO substrates as shown in Figure S1 in the Supporting Information. Therefore, we analyzed the layer thickness and oxidation state with X-ray photoelectron spectroscopy (XPS). XPS measurements on ITO/CuO_x layers on glass show the presence of In and Cu in the survey spectra as shown in **Figure 2**a. Keeping in mind that XPS is a surface sensitive technique with a detection depth up to 5–10 nm and considering the fact that the In substrate peak is visible and the In $3d_{5/2}$ signal at 444 eV has a substantial peak intensity relative to the Cu $2p_{3/2}$ signal at 933 eV, we conclude that we either have a very thin CuO_x film or some islands of CuO_x. Figure 2b shows a closer look at the core-level spectra, which reveals that the Cu is present in oxidation state +I as shown by the peak component Cu $2p_{3/2}$ at 932.5 eV (green) and oxidation state +II, as shown by the second component at 934 eV (red) and the satellite peaks between 941 eV and 943 eV.[43] In order to determine the type of CuO_x layer growth on the ITO surface and to measure the thickness t, we further analyze the CuO_x layer on ITO by angle-resolved XPS (ARXPS), looking at the angular dependence of the peak intensities of layer and substrate material. In addition, we apply a complementary method focusing on the background intensities instead.

In the ARXPS experiment we measured the signal of In and Cu at different angles. The data and more details on the analysis are as described in Figure S2 in the Supporting Information. In order to determine the thickness of the CuO_x layer, we then use a fit to the angularly resolved data with an overlayer model developed by Paynter.[44] By analyzing the ratio of the In 3d and Cu 2p peak intensities at different measurement angles we find three scenarios that are consistent with the angularly resolved data. 1) The CuO_x exists as an atomic monolayer on top of the ITO with a thickness of about 5 Å and a fractional coverage of 7%. 2) A very thin uniform layer of CuO_x with a sub-monolayer thickness or 3) a mixed CuO_x/ITO layer, representing the situation that CuO_x diffused into the ITO layer. Scenario 2 can be immediately discarded since it is not possible to have a uniform film of sub-monolayer thickness.

In order to distinguish between the hypothesis of an island growth and the possibility of having a mixed layer, we use the model described by Tougaard.[45–47] In this model Tougaard explains the importance of the background shape of the peak for the analysis and how the background changes due to the positioning of the material in question from being on the surface or below the surface as described in Figure S3 in the Supporting Information. One simple application of this method is to check the ratio of the peak area A_p to the background intensity B at an energy position 30 eV above the peak (when given on a binding energy scale). If this ratio is higher than 30, the material is located on the surface. Our calculation of the ratio A_p/B being 37 as shown in the Supporting Information, gives us an indication that the CuO_x is indeed located on the surface of ITO. This conclusion is supported by the same analysis of the In peak resulting in $A_p/B = 22$, which according to Tougaard affirms that its signal is originating neither from a surface only nor from a buried material. The ratio $A_p/B = 22$ for the In peak is only possible if the CuO_x is contained in small islands leaving most of the ITO uncovered.

We can conclude from the XPS analysis that the CuO_x is present as thin islands of 5 Å thickness and covering only 7% of the ITO substrate surface. In addition, we tried to modify the process by Rao et al.[26] by increasing the precursor concentration in order to increase the surface coverage. However, preliminary test with these devices showed decreasing performance with higher CuO_x precursor concentrations, as shown in Figure S4 in the Supporting Information. Interestingly, in combination with our perovskite process this process leading to a low coverage still results in the best performance for thin film CuO_x compared to samples having a higher concentration of the precursor solution. While the exact structural properties of this layer or surface modification are difficult to determine, we can still study the functional properties of this anode stack. Note that for simplicity, we will continue referring to the result of the $Cu(acac)_2$-based process as "CuO_x layer."

Ultraviolet photoelectron spectroscopy (UPS) allows us to determine the valence-band edge and the work function (Φ) present at the surface of different layer stacks. **Figure 3**a–c illustrates the energy levels relative to the vacuum level (E_{vac}) derived from UPS measurements as shown in Figure S9 in the

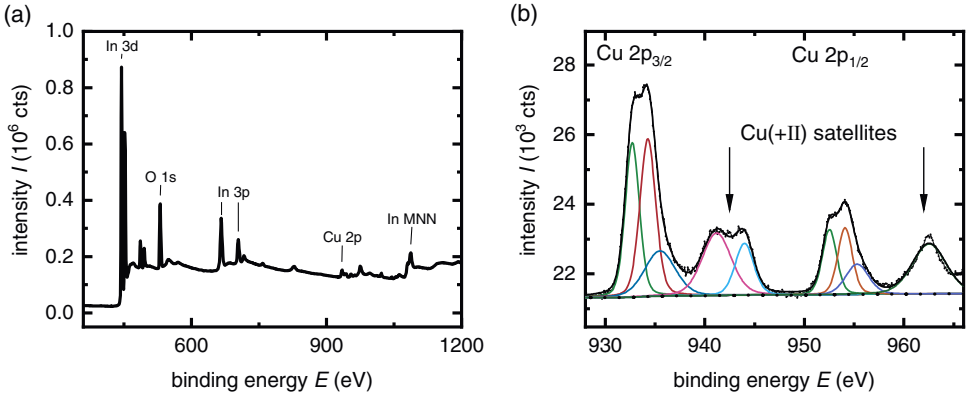

Figure 2. X-ray photoelectron spectroscopy of the solution-processed films. a) Survey spectrum of CuO_x on an ITO substrate, showing both the Cu 2p peak and the In 3d peak. The Cu 2p peak is small in comparison to the In 3d peak suggesting either a thin layer of CuO_x or an island growth of CuO_x on top of ITO. b) Cu 2p spectra showing the different oxidation states of Cu: Cu + I (Cu_2O) and Cu + II (CuO, satellites).

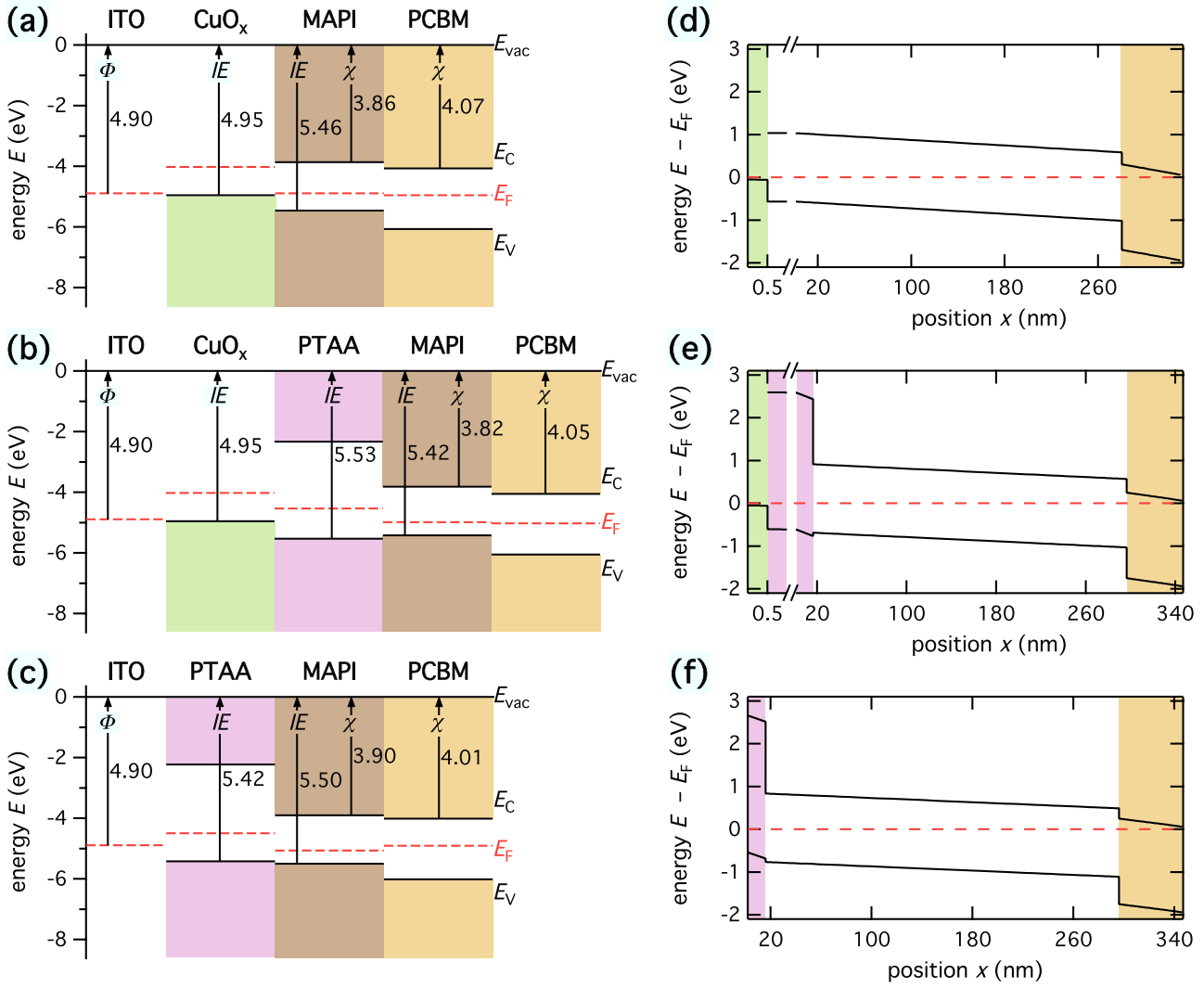

Figure 3. Schematics of the energy-level diagrams derived from UPS measurements, where Φ represents work function, χ the electron affinity, IE the ionization energy, E_{vac} the vacuum energy, E_C conduction-band energy, E_F the Fermi-level energy, and E_V represents the valence-band energy. These measurements were done for the different layers at the different stages of the device processing using different HTLs in the device, a) CuO_x, b) CuO_x/PTAA bilayer, and c) PTAA. SCAPS[48] simulated band diagrams from UPS measured work functions and electron affinities are shown in (d)–(f) that correspond to the UPS diagrams shown in (a)–(c), respectively.

Supporting Information. We measured the work function and ionization energy (valence-band edge relative to the vacuum level) for different layer stacks. We started with glass/ITO followed by glass/ITO/HTL, glass/ITO/HTL/MAPI and finally glass/ITO/HTL/MAPI/PCBM. The ionization energy and work function of each layer was determined from the sample stack that ends on that specific layer and therefore indicates the energy levels at the surface of the respective stack. The electron affinities χ, i.e., the positions of the conduction-band edges relative to vacuum, were then determined using the bandgaps of the different layers. We use the following bandgaps for the calculation of χ from the UPS measurements: 3.2 eV for PTAA,[49] 1.6 eV for MAPI, and 2 eV for PCBM.[50]

The UPS data presented in Figure 3a–c allow us to determine only the energy levels of the surfaces of the individual layers, which do not necessarily agree with the situation of the buried interfaces after they are brought into contact with subsequent layers. In order to understand the functionality of the layers in the solar cell, we used a numerical device simulator (SCAPS) to generate an estimate of the equilibrium-band diagram based on the UPS data. Here, it is important to note that the electron affinities of the different layers will dictate the alignment of the conduction-band edges in the final layer stack. However, the position of the equilibrium-Fermi level does not necessarily coincide with the work functions measured by UPS. Instead, charge-carrier injection from layers with higher electron (or hole concentration) into layers with lower concentrations will strongly affect the position of the Fermi level. For ITO which is much more conductive than the other layers (except Ag), it is the work function that matters and that sets the position of the Fermi level of the device stack on the anode side. The next layers are all basically undoped based on the UPS measurements. Even though the Fermi level is not always in the middle of the bandgap, it is always more than 460 meV away from the

nearest band edge which implies that the equilibrium-majority carrier concentrations in all these layers are negligibly low relative to the concentrations of electrons or holes that are injected from the adjacent layers. Only the work function of the final Ag layer that is not shown in Figure 3a–c will again set the position of the Fermi level. Thus, if we want to use the UPS data to draw equilibrium-band-diagrams for a tentative understanding of band alignment, we have to use the conduction- and valence-band offsets of the HTL, absorber and ETL layers as the decisive quantities to understand the band alignment. In contrast, the position of the work function in panels in Figure 3a–c becomes irrelevant except for the ITO and the Ag (see Section S5 in the Supporting Information).

SCAPS[48] is a software to solve 1D continuity equations for electrons and holes as well as the Poisson equation that relates the space charge with the electrostatic potential. We used SCAPS to numerically calculate the tentative band diagrams shown in panels of Figure 3d–f based on the UPS data presented in panels of Figure 3a–c assuming a work function of 4.1 eV for the BCP/Ag cathode.[51,52] One of the most critical parameters to connect the band diagrams with the functionality of the device is the ITO work function. However, literature reports have shown a huge range from 4.3 to 5.2 eV, depending on the preparation of the sample, the cleaning method, the measurement process and the UV intensity during the UPS measurement.[53] In our case, we measured a work function of 4.9 eV for an ITO film on a glass substrate with the O_2-plasma ex-situ cleaning step performed shortly before transfer to the UHV system for the UPS measurement. The resulting built-in voltage from these values of the three devices is (only) 0.8 V, which is substantially smaller than all V_{oc}s of the different devices and is not compatible with the *JV* curves shown in Figure 1b and the performance of the devices. At such a low built-in voltage, one would expect S-shaped *JV* curves that (at least after photoactivation of the perovskite) we do not observe in experiment.[54,55] Hence, we most likely have a higher ITO work function and a higher V_{bi} in the finished devices that we cannot explain with our UPS data.

In the following, we will briefly explain the consequences of an insufficiently high ITO work function on recombination at the perovskite-anode interface. The measured work function of 4.9 eV for ITO is substantially smaller than the ionization energy *IE* of the MAPI absorber layer (average IE_{MAPI} = 5.42 eV), as for the whole range of literature values for the ITO work function cited above (4.2–5.2 eV), there will still be a considerable difference between the work function and the *IE* of MAPI. This energy difference between the work function of ITO and the valence-band edge of MAPI implies that the Fermi level at the HTL/MAPI interface should be quite far away from the MAPI valence-band maxima, which should therefore lead to a comparably low concentration of majority carriers (holes) at the HTL/MAPI interface. The product

$$n_0 p_0 = n_i^2 = N_C N_V \exp\left(\frac{-E_g}{kT}\right) \quad (1)$$

of electron and hole concentrations is constant in equilibrium. Here, n_0 and p_0 are the electron and hole concentrations in thermal and chemical equilibrium, n_i is the intrinsic charge-carrier concentration, N_C and N_V are the effective densities of state of the conduction and valence band, E_g is the bandgap of MAPI, and kT the thermal energy. Ideally, the majority-carrier concentration at an interface is as large as possible and the minority-carrier concentration negligibly small. An insufficiently high work function of the ITO will however lead to a (relative) low equilibrium concentration $p_0 << N_V$ of holes at the interface to the HTL implying that the minorities (electrons) will have a relatively high-equilibrium concentration $n_0 = n_i^2/p_0$. The high minority-carrier concentration would suggest increased surface-recombination rates $S_n \times n$ for a given surface-recombination velocity S_n and quasi-Fermi level splitting ΔE_F at the HTL/MAPI interface. These increased recombination rates would be true for all three configurations, i.e., even for the PTAA/MAPI interface that was previously shown to cause extremely low voltage losses.[14] A key difference between the band diagrams in Figure 3e and f with PTAA and the one in Figure 3d without PTAA is however, that the PTAA should block electrons from diffusing toward the ITO and recombining at the ITO/HTL interface. Given that the used CuO_x recipe only produces island growth with low coverage and a thickness way below tunneling distance, this argument does not hold for the band diagram in Figure 3d. Here, electrons should be able to tunnel from the MAPI directly to the ITO and recombine there. Thus, the ITO/CuO_x/MAPI interface should exhibit substantially higher levels of nonradiative recombination than stacks that involve PTAA.

On the cathode side (right) of the three band diagrams in Figure 3, we do not observe substantial differences. However, we note that the electron affinities and ionization energies of the MAPI layers are slightly different depending on the substrate leading to differences in the band alignment at the MAPI/PCBM interface. The MAPI grown on the ITO/PTAA substrate has the largest electron affinity and therefore the smallest offset to the PCBM (see Figure 3c–f), which should therefore result in the energy-level alignment with the lowest voltage losses among these three cases. This difference in the energy levels of the MAPI implies that the front interface (anode), being also the growth substrate for the absorber layer, could also affect the recombination at the back interface (cathode).

2.2. Solar Cell Fabrication and Characterization

Subsequently, we fabricated perovskite solar cells using the three stacks previously investigated by the UPS measurements shown in Figure 3. The layer thicknesses were ≈14 nm for PTAA, ≈280–300 nm for the MAPI layer, ≈50 nm for PCBM, ≈8 nm for BCP and 80 nm for the Ag contact. Representative *JV* curves of these devices are shown in Figure 1b and the photovoltaic parameters for forward (solid line) and reverse scan (dashed lines), at a scan speed of 100 mV s^{-1}, are shown in **Table 1**.

The perovskite solar cell using CuO_x as HTL shows a low fill factor *FF* (58%). The fill factor increases substantially in the presence of PTAA, whether alone or in a bilayer with CuO_x (73%). The short-circuit current J_{sc} stays almost the same for the three different types of devices (≈19 mA cm^{-2}). As for the

Table 1. Photovoltaic parameters of the solar cell devices measured with a class AAA solar simulator. The first value is always for a forward scan and the number behind the slash is for the reverse scan.

Device	V_{oc} [V]	J_{sc} [mA cm^{-2}]	*FF* [%]	*PCE* [%]
CuO_x	1.06/1.05	19.0/19.4	58.2/59	11.7/11.9
CuO_x/PTAA	1.15/1.15	19.2/19.0	72.9/75.8	16.1/16.0
PTAA	1.26/1.26	18.1/18.2	72.1/76.8	16.5/17.7

open-circuit voltage V_{oc} the CuO_x devices exhibits the lowest V_{oc} of 1.05 V, whereas the highest V_{oc} (1.26 V) is observed for the PTAA-based device. The high V_{oc} for the devices made with PTAA, whether alone or in a bilayer with CuO_x, was reached after preconditioning of the devices via light soaking (see Figure S10 in the Supporting Information), while the solar cells without PTAA did not show a significant light-activation effect.

The key result from the *JV* curves is that devices with pure CuO_x as HTL are indeed substantially worse in terms of V_{oc} than pure PTAA devices. We had already anticipated this result while discussing the equilibrium-band diagrams shown in Figure 3. A tentative explanation for this outcome would then be that the CuO_x/MAPI interface is not suppressing recombination of electrons at this interface.

2.3. Theory of Recombination and Photoluminescence

A method to verify or falsify the hypothesis that the CuO_x/MAPI samples suffer from substantially increased surface recombination at the CuO_x/MAPI interface is based on measuring the luminescence of different layer stacks with and without charge-transport layers.[16,17] In order to understand how photoluminescence introduce after photoluminescence (PL) can be used to better understand recombination and open-circuit voltage losses, we first give a brief introduction into the theory of recombination and luminescence. Recombination rates are made up of three contributions, the recombination coefficients, the equilibrium charge-carrier concentrations and the quasi-Fermi level splitting or voltage. For instance, the rate of radiative recombination could be written as

$$R_{\mathrm{rad}} = k_{\mathrm{rad}} n_0 p_0 \exp\left(\frac{\Delta E_{\mathrm{F}}}{kT}\right) \tag{2}$$

where $n_0 p_0 \propto \exp\left(-E_{\mathrm{g}}/kT\right)$ (see Equation (1)). Here, the radiative recombination coefficient k_{rad} contains information about the charge-carrier kinetics of radiative recombination, the equilibrium concentrations n_0 and p_0 contain information about the bandgap E_{g} (i.e., the enthalpy of the free carriers in a single semiconductor without charge-transport layers) and ΔE_{F} is the quasi-Fermi level splitting, i.e., the free energy of the electron–hole pairs. In addition to radiative recombination, other recombination mechanisms such as Shockley–Read–Hall recombination in the bulk or at interfaces will exist in films and devices and each of them could be written as a product of these three contributions as done in Equation (1).

At a given light intensity and at open-circuit conditions, the rate of generation will be fixed and equal to the sum of all recombination rates. Thus, any additional recombination processes beyond radiative recombination will reduce the quasi-Fermi level splitting that can be achieved. For a solar cell, the reduced quasi-Fermi level splitting will lead to a reduced open-circuit voltage. In most types of perovskite solar cells, $\Delta E_{\mathrm{F}} = qV_{\mathrm{oc}}$ will hold to a good accuracy.[56] In order to study the origin of losses in open-circuit voltage in films or layer stacks it is useful to have a contactless method of measuring the quasi-Fermi level splitting. Photoluminescence is such a contactless method, because any increase in the factor $\exp(\Delta E_{\mathrm{F}}/kT)$ will lead to a linear increase in the rate of radiative recombination (see Equation (2)) and hence an increase in the photoluminescence. Thus, the photoluminescence flux ϕ_{PL} will scale like

$$\phi_{\mathrm{PL}} \propto \exp\left(\frac{\Delta E_{\mathrm{F}}}{kT}\right) \tag{3}$$

with the quasi-Fermi level splitting ΔE_{F}.

In the presence of electron- or hole-transport layers that form interfaces with the perovskite-absorber layer, the luminescence is often substantially reduced relative to the case of a bare perovskite film on glass.[16,17] This reduction in luminescence must originate from additional recombination at the perovskite/charge-transport-layer interface. For our device geometries there are two relevant types of interfaces, where recombination has to be treated in a slightly different way. The first type is a junction between a metal or a metal oxide (such as ITO) and a semiconductor (such as MAPI) where the recombination is only determined by the minority-carrier concentration and the surface-recombination velocity S_{n}. The surface-recombination rate (per area and time) at, e.g., the ITO/MAPI junction would be given by $R_{\mathrm{S}} = S_{\mathrm{n}} n_{\mathrm{MAPI}}$, where n_{MAPI} is the concentration of electrons in MAPI and S_{n} is the surface-recombination velocity for electrons at this junction. The second type is a heterojunction between two semiconductors (i.e., MAPI and PCBM), where the recombination happens between an electron in the PCBM and a hole in the MAPI. Both densities (of electrons and holes on either side of the interface) may change with voltage and illumination. In addition, the interface may be in high or in low level injection, i.e., it is not a priori clear whether we have an excess of electrons or holes at the MAPI/PCBM interface. In order to distinguish between the two types of recombination, we will refer to the first one as surface recombination in analogy to the well-studied process of surface recombination at metal-semiconductor interfaces, while we will refer to the second process of recombination across an interface of two semiconductors as interface recombination.

Interface recombination is typically due to a defect-assisted processes that can be described in a similar way as Shockley–Read–Hall recombination in the bulk. The recombination rate R_{int}, e.g., at a MAPI/ETL interface can therefore be written as

$$R_{\mathrm{int}} = \frac{n_{\mathrm{ETL}} p_{\mathrm{MAPI}} - n_{\mathrm{i,int}}^2}{n_{\mathrm{ETL}}/S_{\mathrm{p}} + p_{\mathrm{MAPI}}/S_{\mathrm{n}}} \tag{4}$$

where $n_{\mathrm{i,int}}^2 \propto \exp\left(-E_{\mathrm{int}}/kT\right)$ and R_{int} is a rate per surface area. Here, S_{n} and S_{p} are the interface-recombination velocities and E_{int} is the interfacial bandgap, i.e., the difference between the

conduction-band edge of the ETL and the valence-band edge of MAPI. Thus, an obvious question that now arises for optimization and better understanding of perovskite/transport-layer interfaces is the question whether kinetic effects (i.e., variations in S_n and S_p) or variations in the energy-level alignment (i.e., variations in E_{int}) most strongly affect recombination. If variations in energy-level alignment are the dominant mechanism, alternative transport layers with different energy levels are required.[57] If variations in S_n and S_p affect recombination most strongly, defect passivation [58,59] is the most likely approach for better open-circuit voltages.

In general, numerical simulations can be used to study how energy-level alignment and surface-(or interface) recombination velocities affect experimental data such as PL spectra and decays but also photovoltaic performance parameters such as the open-circuit voltage. However, before we make use of numerical simulations, we first illustrate the relation between interface-recombination rates and the quasi-Fermi level splitting analytically. In order to do so, we have to restrict ourselves to a simplified thought experiment and make a few (partly arbitrary) assumptions that only serve to illustrate the effect of one interface on the quasi-Fermi level splitting and therefore the steady-state PL and the open-circuit voltage. The first assumption is $n_{ETL} = p_{MAPI}$, i.e., the interface is in high level injection. Let us also assume that recombination at the interface is dominant and all other recombination processes (perovskite bulk and other interfaces) can be neglected. Then, we can equate the particle flux of photogeneration (G) with the recombination rate per surface area given by Equation (4). We obtain

$$Gd_{MAPI} = R_{int} = \frac{n_{ETL}}{1/S_p + 1/S_n} \tag{5}$$

where d_{MAPI} is the thickness of the absorber layer. For the quasi-Fermi level splitting, we find

$$\Delta E_F = 2kT \ln\left(\frac{Gd_{MAPI}\left(S_n + S_p\right)}{n_{i,int}\, S_n S_p}\right) \tag{6}$$

which can be rewritten as

$$\Delta E_F = E_{int} - 2kT \ln\left(\frac{\sqrt{N_{C,ETL} N_{V,MAPI}}\, S_n S_p}{Gd_{MAPI}\left(S_n + S_p\right)}\right) \tag{7}$$

with $N_{C,ETL}$ being the effective density of states in the conduction band of the electron-transport layer and $N_{V,MAPI}$ the effective density of states in the MAPI layer. Equation (7) has the advantage that it provides a thermodynamic interpretation[60] of the different terms and allows better understanding the relation between energy and open-circuit voltage losses. In Equation (7), ΔE_F represents the free energy and therefore the expected maximum value of qV_{oc} in a device limited by that interface, E_{int} is the enthalpy, and the final term represents the entropy multiplied with temperature. A similar equation can easily be derived for the case of $n_{ETL} \neq p_{MAPI}$.

The ideal interface would minimize the interface-recombination loss either by minimizing the enthalpic losses caused by a difference between the bulk bandgap of the absorber layer and the interfacial bandgap E_{int} or by slowing down interface recombination (lower values of S_n and S_p) which would lead to a reduced entropy generation at the interface. Steady-state luminescence alone cannot distinguish between the losses in enthalpy and the additional entropy related to variations in S_n and S_p. Therefore, we will now first study our samples using steady-state photoluminescence and then in a second step explore the combination of steady-state with transient photoluminescence to explore the possibility to extract additional information from the data that would not be accessible by either of the two techniques alone.

2.4. Steady-State Photoluminescence

We performed steady-state luminescence measurements (ss-PL) on seven different samples representing the three different HTLs with only the absorber, the absorber plus ETL (PCBM/BCP), and the full devices. Note that for samples involving PTAA, the luminescence changes with light soaking and therefore for these samples preconditioning was performed as discussed in Section S7 in the Supporting Information. The *JV* characteristics of the samples were measured immediately before being measured at the ss-PL setup, using a white-light LED (as shown in Figure S10 in the Supporting Information). The implied open-circuit voltage ($V_{oc,imp}$) shown in **Figure 4** is given by the difference of energetic levels of the quasi-Fermi level splitting, when the sample is under illumination. In order to study the quasi-Fermi level splitting as a function of the presence or absence of different interface and charge-transport layers. The same samples were also used for the transient photoluminescence experiments discussed in Section 2.5. Figure 4

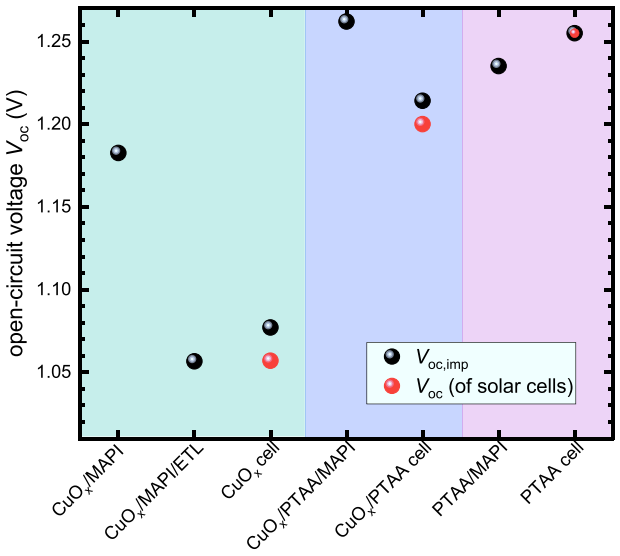

Figure 4. Implied open-circuit voltage $V_{oc,imp}$ derived from the steady-state photoluminescence (ss-PL) measurements for a laser excitation with the equal number of photons as absorbed under one sun AM1.5G illumination (black spheres). The implied open-circuit voltages are determined for a variation of hole-transport materials on seven samples representing the different stages of the device processing. Red spheres indicate the V_{oc} of the three finished solar cell samples measured at the ss-PL setup, where the measured V_{oc} of the PTAA device was used for calibration.

then shows the implied open-circuit voltage ($V_{oc,imp}$) derived from the ss-PL measurement using

$$qV_{oc,imp}(\phi_{PL}) = qV_{oc}(\phi_{sun}) + kT\ln\left(\frac{\phi_{PL}}{\phi_{PL,cell}(\phi_{sun})}\right) \quad (8)$$

where ϕ_{PL} is the photoluminescence of a certain sample in Figure 4 and $\phi_{PL,cell}$ (ϕ_{sun}) is the photoluminescence of the reference cell, whose V_{oc} at that same illumination is known. We assume that for the cell with the highest V_{oc}, namely, the one in the PTAA stack, the quasi-Fermi levels are flat at open circuit and the luminescence obtained for this cell at the equivalent of one sun illumination is therefore used to calibrate the voltage axis for all other samples.[56]

Figure 4 shows that the CuO_x/MAPI interface by itself is not the main culprit leading to the reduced V_{oc} and efficiency of the solar cells shown in Figure 1b. The $V_{oc,imp}$ of the CuO_x/MAPI sample (1.18 V) is reduced relative to the other two samples. This reduction is about 77 mV in $V_{oc,imp}$. This reduction is relatively stable over the different measured batches. The implied $V_{oc,imp}$ that was measured for the different batches had a range of 1.17–1.22 V for CuO_x/PTAA samples and 1.23–1.26 V for PTAA cells samples, however $V_{oc,imp}$ measured for the CuO_x cell samples was always at ≈1.05 V, where a substantial reduction in luminescence is observed when the electron-transport layer (PCBM/BCP) is deposited onto the layer stack and this reduction still remains after adding the Ag back contact.

We observe a similarly high $V_{oc,imp}$ for the HTL/MAPI samples, namely with CuO_x/PTAA ≈1.26 V and with PTAA/MAPI (≈1.24 V). However, for the completed stacks the sample with CuO_x/PTAA HTL has a slightly lower $V_{oc,imp}$ (1.22 V) compared to the stacks with PTAA as HTL which reaches ≈1.255 V.

To conclude, Figure 4 shows that the differences observed in the *JV* curves of the solar cells are also visible in the photoluminescence measurements. The samples containing PTAA show high luminescence in all situations shown. The samples with CuO_x (and no PTAA) show a substantial reduction in luminescence relative to the PTAA-based samples. This reduction happens apparently not only at the CuO_x/MAPI interface but also at the MAPI/PCBM interface. These results were unexpected giving that the large band offset at the CuO_x/MAPI interface does not lead recombination rates as high as expected.

2.5. Transient Photoluminescence

Transient photoluminescence (tr-PL) is frequently used in perovskite solar cell research.[7,8,14,16,61–68] However, except for the simplest case of a perovskite film on glass, there is only a limited amount of research[69] that attempts to do a quantitative analysis of tr-PL data on layer stacks or devices that would actually correlate well with device parameters such as the open-circuit voltage. In case of a perovskite layer on glass, tr-PL is affected by generation and recombination processes and the information obtained by both methods is similar. For instance, it has been shown that using parameters extracted from analysis of the tr-PL allows calculating the quasi-Fermi level splitting which is a key information that can also be extracted from steady-state PL.[70]

In the presence of charge-extracting interfaces, discriminating between entropic (variations in surface-recombination velocities) and enthalpic (i.e., variations in band offsets) contributions to recombination losses is more difficult. The difficulties in analyzing tr-PL on perovskite-transport layer combinations are mainly due to the fact that the transient photoluminescence in the presence of interfaces is affected by the majority-charge carriers diffusing to an interface and transferring to the electron- or hole-transport layer. This process takes a finite amount of time and affects the transient at early times, because it reduces the concentration of electron–hole pairs in the absorber layer. In addition, charge may accumulate in the electron- or hole-transport layers and thereby create an electric field that slows down further charge injection from the absorber to the charge-transport layer.[24] An important difference between ss-PL and tr-PL is the fact that in a steady-state experiment at open circuit, the quasi-Fermi levels are typically flat throughout the absorber, because no currents are flowing. In a tr-PL experiment, currents are flowing, e.g., charge is transferred from the absorber to the electron- or hole-transport layers at early times. Therefore, the two measurement techniques describe slightly different situations.

The tr-PL is affected by a range of parameters but the most important ones at a given interface are

1) the velocities S_T for transfer of a majority carrier to the transport layer (i.e., an electron from the MAPI conduction band to the PCBM lowest unoccupied molecular orbital LUMO),
2) the surface-recombination velocity S_n for recombination of a carrier in the transport layer with a carrier of opposite sign in the absorber layer (i.e., an electron in the PCBM with a hole in the MAPI),
3) the band offset $\Delta E_{c/v}$ for majority carriers (i.e., the difference between the MAPI conduction-band edge and the PCBM LUMO), and
4) the position of the Fermi level at the interface relative to the band edges.

In order to better understand how a combination of tr-PL and ss-PL may support understanding interface recombination, we first present the tr-PL measurements and then proceed to simulate both sets of experiments.

Figure 5 shows the normalized time-resolved photoluminescence ($\phi_{tr\text{-}PL}$) decay measured for the three types of layer stacks using the same samples as those used for the ss-PL shown in Figure 4. Figure 5a shows the photoluminescence decays for the CuO_x -HTL, Figure 5b for the CuO_x/PTAA HTL and Figure 5c for the PTAA HTL. We note that for all but the two CuO_x/MAPI/PCBM/BCP samples with and without Ag (the two darker green lines in Figure 5a a fast initial and a fairly long second decay are observed. For the two exceptions (the two darker green lines in Figure 5a the CuO_x based stacks with electron- and hole-transport layers applied (see Figure 5a), the decay is very fast approaching the noise level within about 100 ns. The presence of a fast initial decay in PL transients of samples with electron- and/or hole-transport layers likely indicates efficient charge transport (rather than detrimental recombination). The presence of long decays at later times is indicative of slow charge recombination and is indeed observed

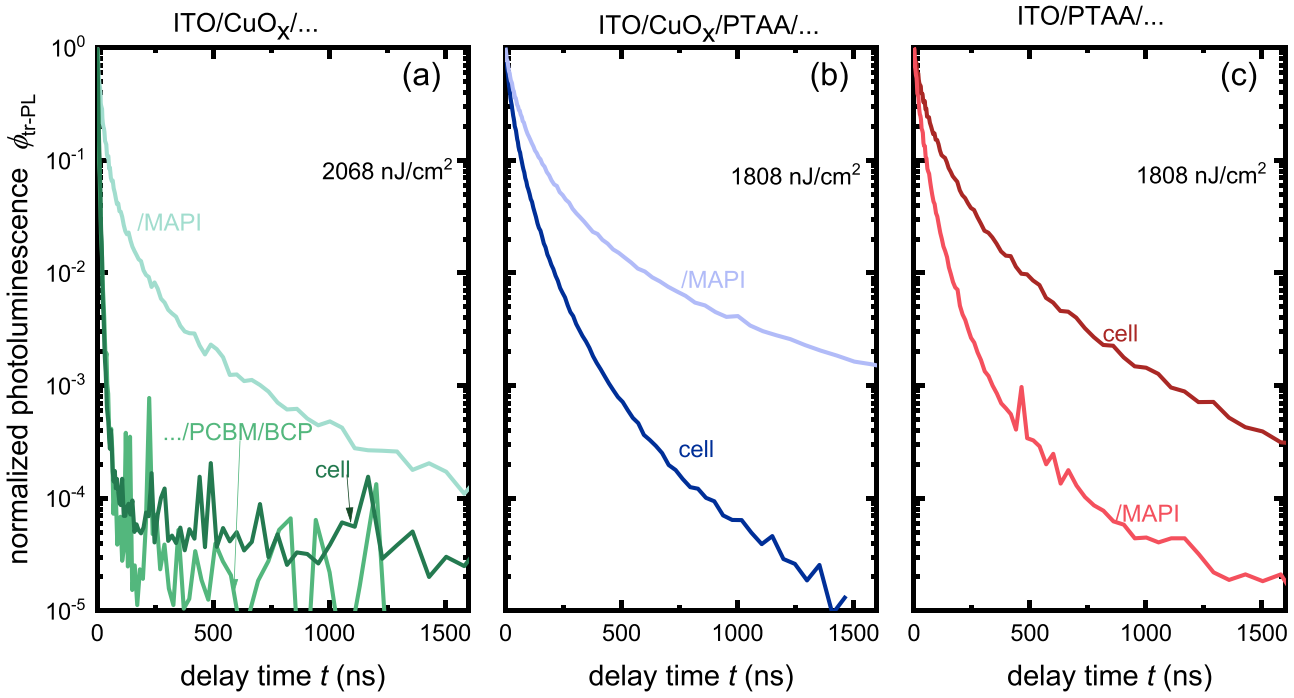

Figure 5. Time-resolved photoluminescence (tr-PL) decay measured for the devices made with different HTLs at different stages of the processing: a) samples with CuO_x as HTL, b) samples with CuO_x/PTAA bilayer as HTL, and c) samples with PTAA as HTL.

consistently for all samples that show high steady-state photoluminescence in Figure 4.

2.6. Simulation of Photoluminescence Transients

Based on the above presented experimental results on the CuO_x-based samples, we now want to study whether the information contained in the ss-PL and the tr-PL measurements on the different samples (with and without electron contact) can offer quantitative insights into the distribution of losses at the two charge-transport interfaces. We choose the CuO_x-based samples for a detailed numerical analysis, because they show substantial losses relative to the ideal case observed with PTAA. In particular, we noted in the discussion of Figure 4 that the losses are difficult to understand given that a substantial drop in $V_{oc,imp}$ occurs at both interfaces while only one interface has been changed (the cathode side of the stack is always nominally the same). Hence, both interfaces seem to contribute to the substantially decreased V_{oc} of the CuO_x-based cell relative to that of the two cells containing PTAA.

We build a model of the ITO/CuO_x/MAPI/PCBM/BCP/Ag stack using the software TCAD SENTAURUS[71] to investigate the decreased V_{oc}. We assume in our model that the thin CuO_x layer modifies the contact properties between the ITO and the MAPI, namely the hole-injection barrier Φ_B and the interface recombination velocity S_R. The BCP layer is not explicitly simulated. Instead, we simulate the BCP/Ag cathode as one layer with a modified work function of 4.1 eV as discussed above. Therefore, for these simulations we omit the CuO_x and implement an ITO/MAPI interface with a modified ITO work function and interface-recombination velocity (see Table S9 in the Supporting Information). The high conductivity of the ITO implies that any spatial variations in the properties of this interface would not lead to considerable spatial variations in electrostatic potential at this interface. The other interface between the MAPI and the PCBM is modeled as a semiconductor heterojunction, with the conduction band offset ΔE_C and recombination mostly happening between the conduction band of the PCBM and the valence band of the MAPI. We assume the trapping and detrapping at this interface to be symmetrical, i.e., the interface recombination velocity as $S_R = S_n = S_p$. The software solves the Poisson equation and the continuity equations for electrons and holes, including charge generation, recombination, drift and diffusion as a function of time and therefore allows us to simulate steady-state and transient PL experiments as well as draw band diagrams of the different situations.

Figure 6 shows the band diagram of our model of the ITO/CuO_x/MAPI/PCBM stack for three different scenarios (ss-PL, tr-PL (@ $t = 0$ ns and tr-PL (@ $t = 200$ ns). The band diagram of the ss-PL (Figure 6a) shows a situation where the quasi-Fermi levels are flat since the charge carriers had enough time to equilibrate. The implied open-circuit voltage is given by the splitting of the quasi-Fermi levels (divided by elementary charge). The splitting of the quasi-Fermi levels depends mainly on the interface properties that are slightly different at the two different contacts. In case of the ITO/CuO_x anode, we only consider the work function of this contact but not, e.g., the position of the conduction band edge of the ITO, because ITO is a degenerate, highly conductive semiconductor and CuO_x is not a full layer. The work function of the anode determines the hole-injection barrier Φ_B, i.e., the difference between the hole quasi-Fermi level and the valence-band edge E_V. In contrast, the PCBM/BCP/Ag cathode features a type II heterojunction at the

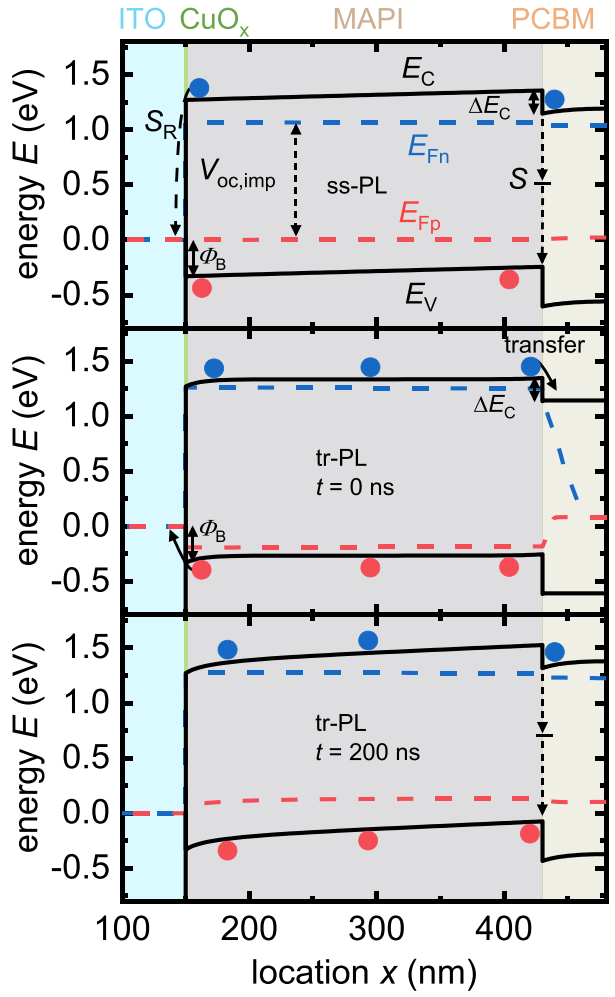

Figure 6. Band diagrams of the ITO/CuO_x/MAPI/PCBM stack showing the different recombination and charge-transfer mechanisms that can happen. a) Steady-state illumination, where the recombination at the MAPI/PCBM interface determines the $V_{oc,imp}$. b) tr-PL situation directly after the laser pulse $t = 0$ s, where we have high electron density in the MAPI, which will transfer to the PCBM and the ITO. c) Band diagram simulated 200 ns after the laser pulse. Now, substantial transfer of electrons to the PCBM has happened resulting in electron accumulation (and band bending) in the PCBM close to the PCBM-Perovskite interface.

MAPI/PCBM interface, where the conduction-band offset ΔE_C is of huge importance, because it affects the enthalpy of the electron–hole pairs recombining via the interface.

In case of the tr-PL at $t = 0$ ns directly after the laser pulse (Figure 6b), we observe a large quasi-Fermi level splitting in the MAPI and a steep gradient of the quasi-Fermi levels at the interfaces which leads to transfer of electrons from the MAPI to the PCBM. Thus, the transfer of electrons to the PCBM is an important process reducing the charge-carrier concentration in the MAPI layer and thereby the PL at short times. Figure 6c depicts the simulated band diagram 200 ns after the pulse, showing that the gradients in the quasi-Fermi levels have diminished. Hence, the band diagram at longer times resembles more closely the steady-state situation shown in Figure 6a.

While the $V_{oc,imp}$ from ss-PL measurements is determined by the recombination rates as discussed in Section 2.3, the tr-PL at short times might also contain information about the charge transfer from the absorber to the transport layers. The assumption that the tr-PL contains information about the charge transfer is confirmed by Figure S15 in the Supporting Information, in which three different band offsets and three different values of S_R lead to the same $V_{oc,imp}$ but different tr-PL decays. The different transients are most likely due to accumulation of charge carriers at the MAPI/PCBM interface. These accumulations are caused by a relatively low interface-recombination velocity, which leads to high electron densities in the PCBM and therefore high coulombic attraction between electrons in the PCBM and the remaining holes in the MAPI. The charge accumulation slows down the rate of charge transfer at the interface.[24]

In order to test how independent the information extracted from steady-state and transient PL datasets are, we performed numerical simulations of the different samples, which allow us to study the effect of charge extraction, charge recombination and band offsets on the carrier concentrations in the perovskite from which we derive the tr-PL and ss-PL. In various ss-PL and tr-PL simulations we varied the surface-recombination velocity S_n and the hole-injection barrier Φ_B at the CuO_x-anode for the ITO/CuO_x/MAPI/PCBM stack and the interface-recombination velocities S_R (assuming that $S_R = S_n = S_p$) and the conduction band offset ΔE_C at the PCBM/MAPI interface. From the steady-state simulations, we calculated the quasi-Fermi level splitting $\Delta E_F = qV_{oc,imp}$. The transient simulations were used to fit data shown in Figure 5a and the root-mean-square error of the fit to the data was analyzed as a figure of merit for the quality of the fits.

Figure 7a shows the comparison of experiment and simulation of an ITO/CuO_x/MAPI stack and investigates the effect of surface-recombination velocity S_n and hole-injection barrier Φ_B (cf. Figure 6, the distance between valence band and Fermi level at the HTL/MAPI interface) on the $V_{oc,imp}$ (lines) and the error plot of the tr-PL. The error plot shows the goodness of the fit between the simulated tr-PL and the measured tr-PL for the ITO/CuO_x/MAPI sample (see Equation (S6) in the Supporting Information used to determine the error). As predicted by Equation (7), Figure 7a shows that lines of equal $V_{oc,imp}$ span the region from high surface-recombination velocity S_n and low hole-injection barriers Φ_B to low S_n and Φ_B. These results can be rationalized by considering that a high $V_{oc,imp}$ requires to have either slow recombination kinetics (small S_n) or a low concentration of charge carriers at the interface (low band offset). Given that changes in the band offset affect the concentration of carriers exponentially, we obtain lines on a plot where S_n is varied logarithmically and the offset is varied linearly as done in Figure 7a.

The lowest error (dark blue regions in Figure 7a) with respect to the experimental PL transient shows the same general tendency, but it is not completely parallel to the lines we obtain for the ss-PL. The same general trend is observed in Figure 7b for the samples that are finished up to the BCP layer (only excluding the Ag back contact), assuming the best fitting parameter from Figure 7a for the CuO_x/MAPI interlayer. Here, the characteristic parameters of the MAPI/PCBM interface are varied and we look at their impact on the fit error and the implied open-circuit voltage. Again, we note that our two observables have the same qualitative but not the same quantitative S_R and the interface offset at the MAPI/ETL interface. These findings sug-

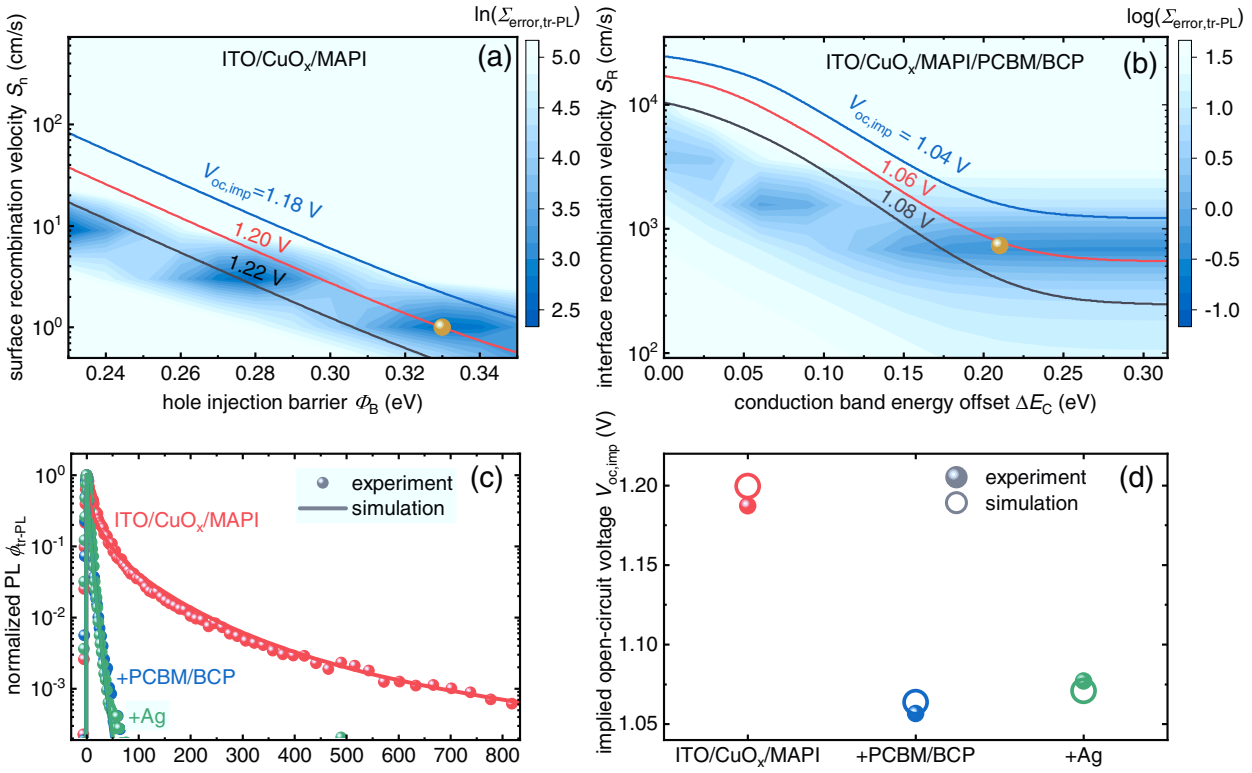

Figure 7. Root-mean-square error Σ_{error} between measured and simulated tr-PL curves superimposed with lines of equal implied open-circuit voltage $V_{oc,imp}$ calculated from steady-state simulations: a) for the ITO/CuO_x/MAPI sample and b) for the ITO/CuO_x/MAPI/PCBM/BCP sample. The superimposed plots show how linearly dependent tr-PL and ss-PL measurements are. The yellow spheres in (a) and (b) mark the scenarios, where low root-mean-square error and $V_{oc,imp}$ overlap the most. c) Normalized tr-PL decay and d) $V_{oc,imp}$ from these best fitting scenarios compared to the experimental data.

gest that it is indeed rather difficult to quantitatively discriminate between entropic and enthalpic contributions to interface-recombination losses in perovskite solar cells. However, we are still able to determine how compatible a certain combination of parameters is with our experimentally accessible observables. The yellow spheres in panels of Figure 7a and b represent the scenarios that give the best fit (smallest error) to all experimental data and these fits are then also presented in panels of Figure 7c and d. For this particular example, we find that the HTL/MAPI interface is strongly energetically misaligned by 330 mV with the surface-recombination velocity being actually quite small (S_n = 1 cm s^{-1}). At the MAPI/ETL interface, again the interface seems to feature a reasonably high band offset of 210 meV (this time at the conduction-band edge) and in addition also higher surface-recombination velocities (733 cm s^{-1}). Due to the high offsets on both sides of the device, substantial concentrations of charges would accumulate at all interfaces of the CuO_x-based solar cell leading to high rates of recombination and therefore substantially reduced open-circuit voltages relative to the PTAA-based reference cells. The key open question that the present paper cannot answer is why exactly the properties of the MAPI/PCBM interface are different depending on whether the layers are deposited on PTAA or not. The fact that the MAPI/PCBM interface can have an extremely low interface-recombination velocity has been previously reported[14] and is also confirmed by the present study (see Figure S14 in the Supporting Information).

3. Conclusion

Interface recombination is one of the key loss processes in most photovoltaic technologies, halide perovskites included.[58,59,72,73] Unfortunately, it is often extremely difficult to find quantitative assays of interface recombination that allow us to disentangle kinetic and energetic influences. In the present study, we focus on the importance of having a good band alignment (low band offsets for majority carriers) and a high built-in voltage.[54] We combine photoelectron spectroscopy, electrical measurements of the open-circuit voltage, steady-state and transient photoluminescence and numerical simulations to gain an improved insight into the efficiency limiting losses at interfaces. We study a set of three different hole-transport layers in a p–i–n type configuration, namely, PTAA, CuO_x, and a CuO_x/PTAA bilayer, which we combine with our lead-acetate-based MAPI process for the highest open-circuit voltages. Two of the investigated hole-transport layers (PTAA and CuO_x/PTAA) work quite well and allow reaching high open-circuit voltages exceeding 1.2 V, while one (CuO_x) falls considerably short in terms of open-circuit voltage. The combination of various spectroscopy methods shows that the poor band alignment at the CuO_x/MAPI interface leads to additional recombination losses relative to the PTAA-containing samples. However, the full extent of the loss is only observed once the PCBM electron-transport layer is deposited. Given that the PCBM forms an interface with very low recombination activity if interfaced with

MAPI grown on PTAA, the data suggests that the recombination rate at the MAPI/PCBM interface is strongly affected by the underlying substrate.

4. Experimental Section

Device Fabrication: Methylammonium iodide (MAI) was purchased from Greatcell Solar. Lead acetate trihydrate ($Pb(CH_3COO)_2{\cdot}3H_2O$, >99.5%) and lead chloride ($PbCl_2$, >99.999%) were purchased from TCI. Poly[bis (4-phenyl)(2,4,6-trimethylphenyl)amine] (PTAA) and bathocuproine (BCP, >99.8%) were purchased from Ossila Ltd. (United Kingdom). [6,6]-phenyl-C_{61}-butyric acid methyl ester (PCBM) was purchased from Solenne (Netherlands). Toluene (T), purity of 99.8%, *N*,*N*-dimethylformamide (DMF, 99.8%), isopropanol (IPA, 99.5%), 1,2-dichlorobenzene (1,2-DCB, 99%), chlorobenzene (CB, 99.8%), and copper acetylacetonate ($Cu(acac)_2$) were purchased from Sigma-Aldrich and used as received.

The prepatterned ITO substrates (2.0 × 2.0 cm^2) were bought from PsiOTec Ltd. and ultrasonically cleaned with soap (Hellmanex III), deionized water, acetone, and IPA in succession for 10 min. Finally, the ITO substrates were O_2-plasma-cleaned before use for ≈12 min (Diener Electronic GmbH + Co. KG, Modell Zepto, 13.56 MHz, 50 W). For the stacks with a CuO_x layer, a solution of $Cu(acac)_2$ (1.5 mg mL^{-1} in DCB) was spin-coated on ITO in air with 4000 rpm speed for 30 s (with a ramping rate of 2000 rpm s^{-1}), followed by an annealing step in air at 80 °C for 20 min. The samples were removed from the hotplate to cool down and then washed with methanol 99.99% purchased from Sigma Aldrich via spin coating at 3000 rpm speed for 60 s (with a ramping rate of 1500 rpm s^{-1}). The samples were then transferred to a glovebox with N_2 atmosphere (MBraun).

For the samples with PTAA layer, ≈110 µL PTAA (2 mg mL^{-1} in toluene) solution was spin-coated onto the ITO substrates or in the case of bilayer on top of the CuO_x layer with a two-consecutive step program at 500 rpm for 4 s (with a ramping rate of 500 rpm s^{-1}) and 4500 rpm for 20 s (with a ramping rate of 900 rpm s^{-1}). Then the samples were thermally annealed at 110 °C for 10 min and afterward cooled down to room temperature. The PTAA layer thickness is around ≈14–16 nm.

The perovskite precursor solution, prepared by mixing $Pb(CH_3COO)_2{\cdot}3H_2O$ (0.54 M), $PbCl_2$ (0.06 M) and MAI (1.8 M) in DMF, was stirred at room temperature overnight and filtered with a 0.45 µm PTFE filter prior to use. To fabricate the perovskite layer, the precursor solution was preheated at 75 °C and ≈140 µL was spin-coated on the top of PTAA or CuO_x layer by a two-consecutive step program at 2000 rpm for 5–10 s (with a ramping rate of 500 rpm s^{-1}) and 6000 rpm for 15 s (with a ramping rate of 1000 rpm s^{-1}). The samples were immediately annealed on a hot plate at 75 °C for 2 min. Afterward they were cooled down to room temperature for 30 min. As an electron-transport layer (ETL), a PCBM solution (≈80 µL, 20 mg mL^{-1} in CB preheated to 75 °C) was spin-coated on the top of perovskite layer at a speed of 1200 rpm for 60 s (with a ramping rate of 400 rpm s^{-1}). For the drying of the PCBM layer the samples were left in an open petri dish for 1 h, without additional annealing. Then, 120 µL BCP was spin-coated on the samples (0.5 mg mL^{-1} in IPA) at 4000 rpm for 30 s (with a ramping rate of 800 rpm s^{-1}). Finally, 80 nm Ag was thermally evaporated in a separate vacuum chamber (<5 × 10^{-6} Pa) through a metal shadow mask to define an aperture area of 0.16 cm^2 by the overlap of the ITO and Ag.

Material Characterization: The XPS/UPS system is a MULTIPROBE MXPS system from Scienta Omicron with an ARGUS hemispherical electron spectrometer and part of the JOSEPH cluster system in the research center Jülich.

XPS: The XPS system used an XM 1000 AlK_α X-ray source operated at 300 W. The resultant spectra were collected in constant Analyzer-Energy (CAE) mode with path energy of 100 eV for the survey spectrum and 20 eV for the high-resolution spectra. Intensities were determined by measuring the area of each peak, after subtracting a Shirley-type background and fitting the experimental curve to a combination of Lorentzian and Gaussian lines with a fixed proportion of 30:70. Binding energies were referenced to the C 1s peak at 284.8 eV.

UPS: Ultraviolet photoelectron spectroscopy (UPS) measurements were done on the same samples with the same setup using a He I discharge lamp (21.22 eV, HIS13, Focus GmbH) for excitation, and a bias voltage of 9 V was applied to the samples. The Fermi level, measured on Au, was used to calibrate the spectra. More detailed explanation of both XPS and UPS measurement methods is described in a previous paper.[14]

For all the following measurements, the samples were mounted inside a sealed, nitrogen-filled sample box and excited from the glass side.

JV: The three devices presented in Figure 1b were measured using a class AAA solar simulator. The photovoltaic parameters measurements were reached after preconditioning of the devices. This preconditioning was also described in the paper by Liu et al.,[14] where it was shown that a continuous illumination for 10–15 min using an LED light source fixed to 1 Sun illumination is needed in order to stabilize the V_{oc}.

LED-Solar Simulator Measurements: this solar simulator, integrated inside a glovebox, was used to measure *JV* curves and for the activation of the samples before being measured at the ss-PL setup. The setup was equipped with a white LED (Cree Xlamp CXA3050), whose illumination was calibrated to yield the same J_{sc} on the investigated cell stacks as an AM1.5 sun simulator A Keithley, model 2450 was used as a source measurement unit.

ss-PL: For the steady-state PL (ss-PL) measurements, the samples were excited with a monochromatic continuous wave laser with a wavelength of 532 nm (coherent sapphire). The laser beam is expanded and reaches the sample with a square-shaped beam with a size of 5.3 × 5.3 mm, illuminating the complete cell area of 16 mm^2. The resulting luminescent light was detected by a spectrometer (Andor Shamrock 303, with a grating of 150 lines mm^{-1} and a central wavelength of 800 nm) connected to a cooled Si (deep depletion) CCD camera (iDus series). In order to get an equivalent number of photons as absorbed under the illumination of the AM1.5G spectrum, the laser power was converted into a photon flux and correlated to the corresponding photon flux of the AM1.5G solar spectrum that was absorbed by the perovskite material with 1.6 eV bandgap assuming the absorptance equals one (1.5871 × 10^{17} cm^{-2} s^{-1}). The corresponding laser power density is 59.3 mW cm^{-2}. Further details are described in the article by Liu et al.[14] The stability of the samples was monitored by measuring the PL intensity at 1 Sun equivalent laser power at the start and end of each set of measurements of ss-PL and tr-PL. Both measurements were done on the same samples consecutively, accompanied by measurements of *JV* characteristics with white light LED before and after the PL measurements.

tr-PL: For the transient photoluminescence, measurements, the samples were excited with a pulsed UV-solid-state laser (100 Hz), which serves as a pump laser for the dye laser. The pumped dye (Coumarin) emits downconverted, pulsed laser radiation of 498 nm. This radiation passes through an optical fiber and impinges at an angle of 30° on the sample surface and illuminates an elliptical shaped spot with dimensions of a = 0.326 mm and b = 0.345 mm (0.353 mm^2). The emitted photoluminescence spectra were focused into a spectrometer (sPEX 270M from Horiba Jobin Yvon). In the spectrometer, the PL beam was diffracted by the grating unit (150 lines mm^{-1}, 500 nm blaze) and spectrally dispersed. The spectrally dispersed signal was then detected with a CCD camera (iStar DH720 from Andor Solis), where the signal was first converted into an electrical signal by a photocathode and amplified by an MCP, to be then back converted using a phosphor screen and finally detected with a CCD chip consisting of an array of 1024 × 256 pixels. The applied power density for the samples with CuO_x as HTL is 2068 nJ cm^{-2}.

Supporting Information

Supporting Information is available from the Wiley Online Library or from the author.

Acknowledgements

The authors acknowledge the Helmholtz Association for funding via the PEROSEED project. S.M. kindly acknowledges the financial support obtained in the framework of DFG Priority Program Perovskites "SPP 2196/1 - Perovskite semiconductors: From fundamental properties to devices." The infrastructural support provided by the University of Cologne is gratefully acknowledged. The authors also thank the Initiative and Networking Fund of the Helmholtz Association for funding of the JOSEPH cluster system via the Helmholtz Energy Materials Characterization Platform (HEMCP).

Conflict of Interest

The authors declare no conflict of interest.

Keywords

angle-resolved XPS, CuO_x, hole-transport layers, nonradiative voltage losses, perovskite solar cells, photovoltaics, ultraviolet photoelectron spectroscopy

Received: February 28, 2020
Revised: May 16, 2020
Published online: June 28, 2020

[1] U. Rau, *Phys. Rev. B* **2007**, *76*, 085303.
[2] R. T. Ross, *J. Chem. Phys.* **1967**, *46*, 4590.
[3] H. J. Snaith, *J. Phys. Chem. Lett.* **2013**, *4*, 3623.
[4] G. Murtaza, I. Ahmad, *Phys. B* **2011**, *406*, 3222.
[5] A. Kojima, K. Teshima, Y. Shirai, T. Miyasaka, *J. Am. Chem. Soc.* **2009**, *131*, 6050.
[6] L. Etgar, P. Gao, Z. Xue, Q. Peng, A. K. Chandiran, B. Liu, M. K. Nazeeruddin, M. Grätzel, *J. Am. Chem. Soc.* **2012**, *134*, 17396.
[7] D. W. deQuilettes, S. Koch, S. Burke, R. K. Paranji, A. J. Shropshire, M. E. Ziffer, D. S. Ginger, *ACS Energy Lett.* **2016**, *1*, 438.
[8] I. L. Braly, D. W. deQuilettes, L. M. Pazos-Outón, S. Burke, M. E. Ziffer, D. S. Ginger, H. W. Hillhouse, *Nat. Photonics* **2018**, *12*, 355.
[9] S. Feldmann, S. Macpherson, S. P. Senanayak, M. Abdi-Jalebi, J. P. H. Rivett, G. Nan, G. D. Tainter, T. A. S. Doherty, K. Frohna, E. Ringe, R. H. Friend, H. Sirringhaus, M. Saliba, D. Beljonne, S. D. Stranks, F. Deschler, *Nat. Photonics* **2020**, *14*, 123.
[10] M. Abdi-Jalebi, Z. Andaji-Garmaroudi, S. Cacovich, C. Stavrakas, B. Philippe, J. M. Richter, M. Alsari, E. P. Booker, E. M. Hutter, A. J. Pearson, S. Lilliu, T. J. Savenije, H. Rensmo, G. Divitini, C. Ducati, R. H. Friend, S. D. Stranks, *Nature* **2018**, *555*, 497.
[11] W. Xu, Q. Hu, S. Bai, C. Bao, Y. Miao, Z. Yuan, T. Borzda, A. J. Barker, E. Tyukalova, Z. Hu, M. Kawecki, H. Wang, Z. Yan, X. Liu, X. Shi, K. Uvdal, M. Fahlman, W. Zhang, M. Duchamp, J.-M. Liu, A. Petrozza, J. Wang, L.-M. Liu, W. Huang, F. Gao, *Nat. Photonics* **2019**, *13*, 418.
[12] K. Lin, J. Xing, L. N. Quan, F. P. G. de Arquer, X. Gong, J. Lu, L. Xie, W. Zhao, D. Zhang, C. Yan, W. Li, X. Liu, Y. Lu, J. Kirman, E. H. Sargent, Q. Xiong, Z. Wei, *Nature* **2018**, *562*, 245.
[13] Y. Cao, N. Wang, H. Tian, J. Guo, Y. Wei, H. Chen, Y. Miao, W. Zou, K. Pan, Y. He, H. Cao, Y. Ke, M. Xu, Y. Wang, M. Yang, K. Du, Z. Fu, D. Kong, D. Dai, Y. Jin, G. Li, H. Li, Q. Peng, J. Wang, W. Huang, *Nature* **2018**, *562*, 249.
[14] Z. Liu, L. Krückemeier, B. Krogmeier, B. Klingebiel, J. A. Márquez, S. Levcenko, S. Öz, S. Mathur, U. Rau, T. Unold, T. Kirchartz, *ACS Energy Lett.* **2019**, *4*, 110.
[15] D. Yang, X. Zhang, K. Wang, C. Wu, R. Yang, Y. Hou, Y. Jiang, S. Liu, S. Priya, *Nano Lett.* **2019**, *19*, 3313.
[16] M. Stolterfoht, C. M. Wolff, J. A. Márquez, S. Zhang, C. J. Hages, D. Rothhardt, S. Albrecht, P. L. Burn, P. Meredith, T. Unold, D. Neher, *Nat. Energy* **2018**, *3*, 847.
[17] V. Sarritzu, N. Sestu, D. Marongiu, X. Chang, S. Masi, A. Rizzo, S. Colella, F. Quochi, M. Saba, A. Mura, G. Bongiovanni, *Sci. Rep.* **2017**, *7*, 44629.
[18] M. Stolterfoht, P. Caprioglio, C. M. Wolff, J. A. Márquez, J. Nordmann, S. Zhang, D. Rothhardt, U. Hörmann, Y. Amir, A. Redinger, L. Kegelmann, F. Zu, S. Albrecht, N. Koch, T. Kirchartz, M. Saliba, T. Unold, D. Neher, *Energy Environ. Sci.* **2019**, *12*, 2778.
[19] J. C. Yu, S. Badgujar, E. D. Jung, V. K. Singh, D. W. Kim, J. Gierschner, E. Lee, Y. S. Kim, S. Cho, M. S. Kwon, M. H. Song, *Adv. Mater.* **2019**, *31*, e1805554.
[20] D. Luo, W. Yang, Z. Wang, A. Sadhanala, Q. Hu, R. Su, R. Shivanna, G. F. Trindade, J. F. Watts, Z. Xu, T. Liu, K. Chen, F. Ye, P. Wu, L. Zhao, J. Wu, Y. Tu, Y. Zhang, X. Yang, W. Zhang, R. H. Friend, Q. Gong, H. J. Snaith, R. Zhu, *Science* **2018**, *360*, 1442.
[21] K. Gao, B. Xu, C. Hong, X. Shi, H. Liu, X. Li, L. Xie, A. K. Y. Jen, *Adv. Energy Mater.* **2018**, *8*, 1800809.
[22] P. Schulz, *ACS Energy Lett.* **2018**, *3*, 1287.
[23] I. Gelmetti, N. F. Montcada, A. Pérez-Rodríguez, E. Barrena, C. Ocal, I. García-Benito, A. Molina-Ontoria, N. Martín, A. Vidal-Ferran, E. Palomares, *Energy Environ. Sci.* **2019**, *12*, 1309.
[24] B. Krogmeier, F. Staub, D. Grabowski, U. Rau, T. Kirchartz, *Sust. Energy & Fuels* **2018**, *2*, 1027.
[25] S. A. Kulkarni, T. Baikie, P. P. Boix, N. Yantara, N. Mathews, S. Mhaisalkar, *J. Mater. Chem. A* **2014**, *2*, 9221.
[26] H. Rao, S. Ye, W. Sun, W. Yan, Y. Li, H. Peng, Z. Liu, Z. Bian, Y. Li, C. Huang, *Nano Energy* **2016**, *27*, 51.
[27] N. Mundhaas, Z. J. Yu, K. A. Bush, H.-P. Wang, J. Häusele, S. Kavadiya, M. D. McGehee, Z. C. Holman, *Sol. RRL* **2019**, *3*, 1800378.
[28] Q. Wang, C. Bi, J. S. Huang, *Nano Energy* **2015**, *15*, 275.
[29] V. M. Le Corre, M. Stolterfoht, L. Perdigón Toro, M. Feuerstein, C. Wolff, L. Gil-Escrig, H. J. Bolink, D. Neher, L. J. A. Koster, *ACS Appl. Energy Mater.* **2019**, *2*, 6280.
[30] P. K. Kung, M. H. Li, P. Y. Lin, Y. H. Chiang, C. R. Chan, T. F. Guo, P. Chen, *Adv. Mater. Interfaces* **2018**, *5*, 1800882.
[31] L. Capasso, M. Camatini, M. Gualtieri, *Toxicol. Lett.* **2014**, *226*, 28.
[32] M. A. Siddiqui, M. Ahamed, J. Ahmad, M. A. Majeed Khan, J. Musarrat, A. A. Al-Khedhairy, S. A. Alrokayan, *Food Chem. Toxicol.* **2012**, *50*, 641.
[33] S. Chatterjee, A. J. Pal, *J. Phys. Chem. C* **2016**, *120*, 1428.
[34] B. A. Nejand, V. Ahmadi, S. Gharibzadeh, H. R. Shahverdi, *ChemSusChem* **2016**, *9*, 302.
[35] T. Waechtler, N. Roth, R. Mothes, S. Schulze, S. Schulz, T. Gessner, H. Lang, M. Hietschold, *ECS Trans.* **2009**, *25*, 277.
[36] Y.-J. Chen, M.-H. Li, J.-C.-A. Huang, P. Chen, *Sci. Rep.* **2018**, *8*, 7646.
[37] Z.-K. Yu, W.-F. Fu, W.-Q. Liu, Z.-Q. Zhang, Y.-J. Liu, J.-L. Yan, T. Ye, W.-T. Yang, H.-Y. Li, H.-Z. Chen, *Chin. Chem. Lett.* **2017**, *28*, 13.
[38] W. Sun, Y. Li, S. Ye, H. Rao, W. Yan, H. Peng, Y. Li, Z. Liu, S. Wang, Z. Chen, L. Xiao, Z. Bian, C. Huang, *Nanoscale* **2016**, *8*, 10806.
[39] L. Liu, Q. Xi, G. Gao, W. Yang, H. Zhou, Y. Zhao, C. Wu, L. Wang, J. Xu, *Sol. Energy Mater. Sol. Cells* **2016**, *157*.
[40] W. Yu, F. Li, H. Wang, E. Alarousu, Y. Chen, B. Lin, L. Wang, M. Hedhili, Y. Li, K. Wu, X. Wang, O. Mohammed, T. Wu, *Nanoscale* **2016**, *8*, 6173.
[41] C. Zuo, L. Ding, *Small* **2015**, *11*, 5528.
[42] X. Miao, S. Wang, W. Sun, Y. Zhu, C. Du, R. Ma, C. Wang, *Scr. Mater.* **2019**, *165*, 134.

[43] B. V. Crist, *Handbook of Monochromatic XPS Spectra*, XPS International, Wiley New York **2000**.
[44] R. W. Paynter, *Surf. Interface Anal.* **1999**, *27*, 103.
[45] S. Tougaard, *Quantification of Surface and Near-Surface Composition by AES and XPS*, CRC Press, Boca Raton, FL **2009**.
[46] S. Tougaard, *Surf. Sci.* **1985**, *162*, 875.
[47] S. Tougaard, *J. Vac. Sci. Technol., A* **1987**, *5*, 1275.
[48] M. Burgelman, P. Nollet, S. Degrave, *Thin Solid Films* **2000**, *361–362*, 527.
[49] S. Ryu, J. Seo, S. S. Shin, Y. C. Kim, N. J. Jeon, J. H. Noh, S. I. Seok, *J. Mater. Chem. A* **2015**, *3*, 3271.
[50] K. Akaike, K. Kanai, H. Yoshida, J. y. Tsutsumi, T. Nishi, N. Sato, Y. Ouchi, K. Seki, *J. Appl. Phys.* **2008**, *104*, 023710.
[51] J. Troughton, M. Neophytou, N. Gasparini, A. Seitkhan, F. H. Isikgor, X. Song, Y.-H. Lin, T. Liu, H. Faber, E. Yengel, J. Kosco, M. F. Oszajca, B. Hartmeier, M. Rossier, N. A. Lüchinger, L. Tsetseris, H. J. Snaith, S. De Wolf, T. D. Anthopoulos, I. McCulloch, D. Baran, *Energy Environ. Sci.* **2020**, *13*, 268.
[52] S. Toyoshima, K. Kuwabara, T. Sakurai, T. Taima, K. Saito, H. Kato, K. Akimoto, *Jpn. J. Appl. Phys.* **2007**, *46*, 2692.
[53] R. Schlaf, H. Murata, Z. H. Kafafi, *J. Electron Spectrosc. Relat. Phenom.* **2001**, *120*, 149.
[54] O. J. Sandberg, J. Kurpiers, M. Stolterfoht, D. Neher, P. Meredith, S. Shoaee, A. Armin, *Adv. Mater. Interfaces* **2020**, *7*, 2000041.
[55] T. Kirchartz, W. Gong, S. A. Hawks, T. Agostinelli, R. C. MacKenzie, Y. Yang, J. Nelson, *J. Phys. Chem. C* **2012**, *116*, 7672.
[56] P. Caprioglio, M. Stolterfoht, C. M. Wolff, T. Unold, B. Rech, S. Albrecht, D. Neher, *Adv. Energy Mater.* **2019**, *9*, 1901631.
[57] D. B. Khadka, Y. Shirai, M. Yanagida, J. W. Ryan, K. Miyano, *J. Mater. Chem. C* **2017**, *5*, 8819.
[58] S. Akin, N. Arora, S. M. Zakeeruddin, M. Grätzel, R. H. Friend, M. I. Dar, *Adv. Energy Mater.* **2019**, *10*, 1903090.
[59] D. Luo, R. Su, W. Zhang, Q. Gong, R. Zhu, *Nat. Rev. Mater.* **2020**, *5*, 44.
[60] T. Markvart, *IEEE J. Photovoltaics* **2019**, *9*, 1614.
[61] D. Song, P. Cui, T. Wang, D. Wei, M. Li, F. Cao, X. Yue, P. Fu, Y. Li, Y. He, B. Jiang, M. Trevor, *J. Phys. Chem. C* **2015**, *119*, 22812.
[62] S.-H. Turren-Cruz, M. Saliba, M. T. Mayer, H. Juárez-Santiesteban, X. Mathew, L. Nienhaus, W. Tress, M. P. Erodici, M.-J. Sher, M. G. Bawendi, M. Grätzel, A. Abate, A. Hagfeldt, J.-P. Correa-Baena, *Energy Environ. Sci.* **2018**, *11*, 78.
[63] W. Nie, H. Tsai, R. Asadpour, J.-C. Blancon, A. J. Neukirch, G. Gupta, J. J. Crochet, M. Chhowalla, S. Tretiak, M. A. Alam, H.-L. Wang, A. D. Mohite, *Science* **2015**, *347*, 522.
[64] E. A. Alharbi, M. I. Dar, N. Arora, M. H. Alotaibi, Y. A. Alzhrani, P. Yadav, W. Tress, A. Alyamani, A. Albadri, S. M. Zakeeruddin, M. Grätzel, *Research* **2019**, *2019*, 8474698.
[65] S. Wu, Z. Li, J. Zhang, T. Liu, Z. Zhu, A. K. Y. Jen, *Chem. Commun.* **2019**, *55*, 4315.
[66] S. Yang, J. Dai, Z. Yu, Y. Shao, Y. Zhou, X. Xiao, X. C. Zeng, J. Huang, *J. Am. Chem. Soc.* **2019**, *141*, 5781.
[67] Q. Wang, E. Mosconi, C. Wolff, J. Li, D. Neher, F. De Angelis, G. P. Suranna, R. Grisorio, A. Abate, *Adv. Energy Mater.* **2019**, *9*, 1900990.
[68] P. Caprioglio, F. Zu, C. M. Wolff, J. A. Márquez Prieto, M. Stolterfoht, P. Becker, N. Koch, T. Unold, B. Rech, S. Albrecht, D. Neher, *Sust. Energy & Fuels* **2019**, *3*, 550.
[69] J. Wang, W. Fu, S. Jariwala, I. Sinha, A. K. Y. Jen, D. S. Ginger, *ACS Energy Lett.* **2019**, *4*, 222.
[70] F. Staub, H. Hempel, J.-C. Hebig, J. Mock, U. W. Paetzold, U. Rau, T. Unold, T. Kirchartz, *Phys. Rev. Appl.* **2016**, *6*, 044017.
[71] https://www.synopsys.com/silicon/tcad/device-simulation/sentaurus-device.html.
[72] P. Schulz, D. Cahen, A. Kahn, *Chem. Rev.* **2019**, *119*, 3349.
[73] C. M. Wolff, P. Caprioglio, M. Stolterfoht, D. Neher, *Adv. Mater.* **2019**, *31*, 1902762.